Batteries & Supercaps

Review
doi.org/10.1002/batt.202200481

Chemistry Europe
European Chemical Societies Publishing

www.batteries-supercaps.org

Special Collection

Microstructure Engineered Silicon Alloy Anodes for Lithium-Ion Batteries: Advances and Challenges

Penglun Zheng,[a, b] Jichang Sun,[a, c] Huaiyin Liu,[a, c] Rui Wang,[a] Chuanbang Liu,[a] Yang Zhao,[d] Junwei Li,[a] Yun Zheng,*[c] and Xianhong Rui*[e]

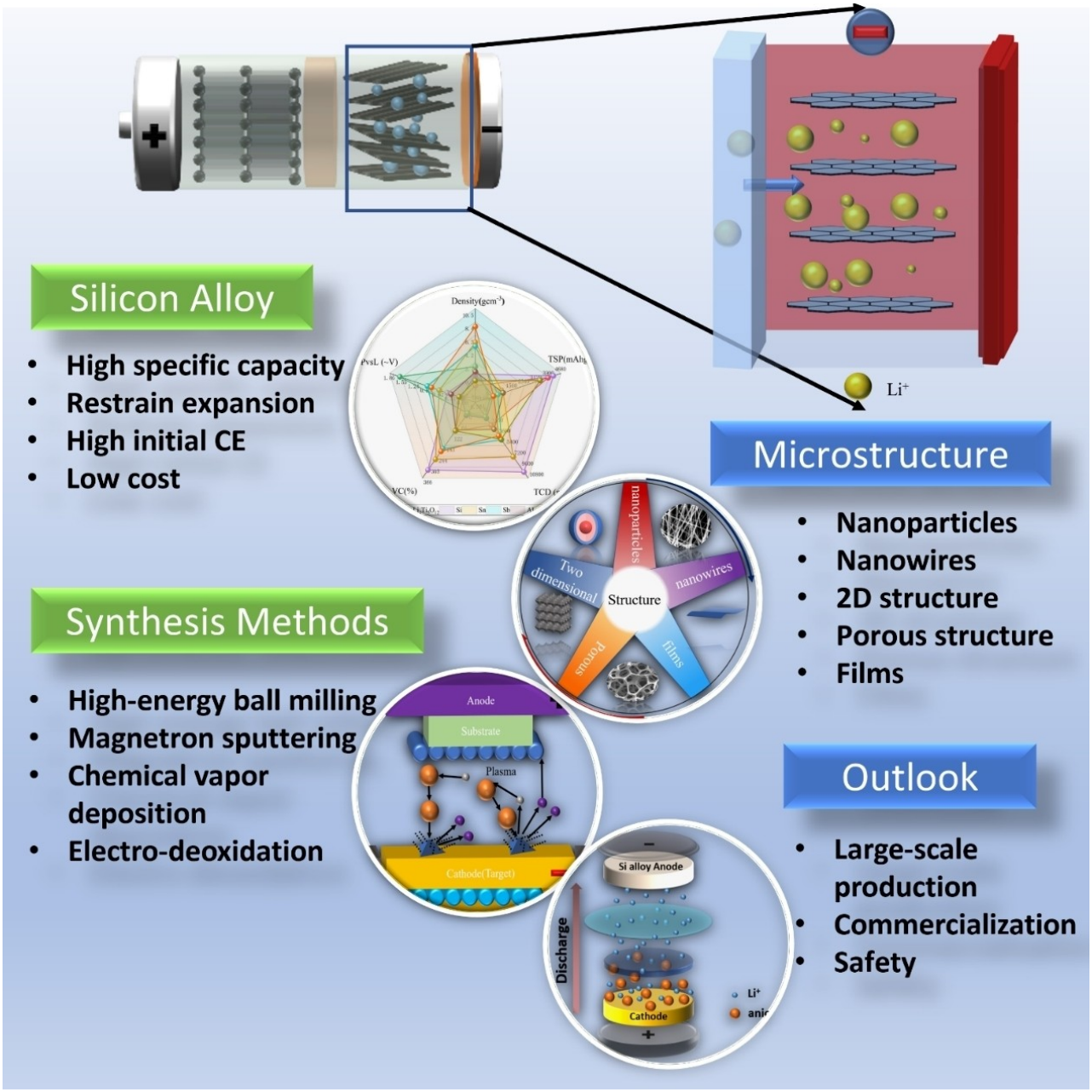

Due to the high theoretical lithium storage capacity and moderate voltage platform, silicon is expected to substitute graphite and serves as the most promising anode material for lithium-ion batteries (LIBs). However, substantial volume change during cycling subjects the silicon anode to electrode pulverization and conductive network damage, extensively limiting its commercial purpose. Strategies, such as alloying, nano-crystallization, and compositing, are developed against these problems. This review introduces the attractive alloying modification method and summarizes the recent advances in microstructure-engineered silicon alloy anodes for LIBs. The electrochemical performances of silicon alloy anodes with various morphologies, such as nanoparticles, nanowires, two-dimensional layered structures, porous structures, and thin films, are discussed in detail. The challenges for the commercial application of silicon alloy anodes are elaborated in the end. This review provides a comprehensive overview and concerns of microstructure-engineered silicon alloy anodes for potential applications in LIBs.

1. Introduction

Lithium-ion battery (LIB) plays a leading role as an energy storage device on account of its high-energy density, good cycle stability, low self-discharge rate, and small voltage decay.[1] LIBs have penetrated the electric vehicle market and are gradually occupying the utility market of power grid energy storage.[2,3] Currently, graphite has been extensively applied as the commercial LIB anode material for its outstanding cycling stability and natural abundance. However, with the emergence of large-scale energy storage demand in future, the commercial graphite anode can no longer meet these requirements owing to the upper limit of its theoretical capacity (372 $mAh\,g^{-1}$).[4–6] Consequently, researchers continue searching for new-generation anode materials with high capacities, appropriate charge/discharge potential, safe operation, and cost-effectiveness in manufacturing and application.[7]

In recent years, the research of anode materials has experienced metal oxides,[8,9] transition metal nitrides,[10,11] composite materials,[12,13] and silicon (Si) anode.[14] Among the various anode candidates, silicon anode arouses wide attention, and has been deemed one of the most prospecting materials to replace graphite. Compared to other anode materials (Figure 1), silicon anode has a high gravimetric, and volumetric capacity;[7] and its appropriate potential improves LIB safety.[15] Furthermore, its rich reservoir (the second most abundant element in the Earth's crust) endows it with low price, good environmental friendliness, and sustainability.[1,5,12,16,17] Despite these advantages, silicon anodes have many drawbacks to be resolved. The most prominent issue is that silicon undergoes ~300% volume expansion during lithium insertion/extraction. This increases the internal stress of the anode, resulting in the surface crack, fracture, and final pulverization of the electrode.[17–19] In addition, the considerable volume change leads to the formation of unstable solid electrolyte interface (SEI) films, eventually causing electrical contact failure inside the electrode and thereby the rapid decline of cycle life.[7,18,20,21] In this respect, researchers proposed versatile designs based on two-dimensional (2D) and three-dimensional (3D) architectures, such as 2D/3D network active materials, 3D conductive skeletons, and 3D collectors.[22] These multi-dimensional structures promote electron and ion transport, increase mass loading,[23] and improve mechanical responses.[21,24] Furthermore, effective approaches have been developed, including artificial SEI film design, robust binder incorporation,[25] carbon coating, and introducing beneficial steps to inhibit silicon anode expansion.[24,26,27] Notwithstanding these silicon-based anodes can maintain morphological completeness to a certain extent, their Coulombic efficiencies are usually insufficient to satisfy the practical requirements.[28] Therefore, alloying elements are involved in silicon anodes to produce silicon-based alloy anodes. Firstly, the Si alloy-based materials can maintain the superior specific capacity of silicon and high initial Coulombic efficiency. Secondly, they inhibit the volume change to a certain extent, alleviating the average capacity decay rate and significantly improving the battery's overall performance. At last, most Si alloy materials have good electrical conductivity.

This paper reviews the recent development of microstructure engineered silicon-based alloy anodes for LIBs. Firstly, we introduce the common synthesis methods of silicon-based alloys and discuss their advantages and disadvantages. Then the effects of these different morphologies of silicon anodes on the LIB performance are described in detail (as schematically shown in Figure 2). Finally, the major challenges with the future development of silicon-based alloy anodes have been prospected. This review emphasizes the importance of microstructure engineering in silicon alloy anodes for practical applications.

[a] P. Zheng, J. Sun, H. Liu, R. Wang, C. Liu, J. Li
College of Civil Aviation Safety Engineering
Civil Aviation Flight University of China
De Yang Shi, Guanghan 618307, P. R. China
[b] P. Zheng
Civil Aircraft Fire Science and Safety Engineering Key Laboratory of Sichuan Province, Civil Aviation Flight University of China
De Yang Shi, Guanghan 618307, P. R. China
[c] J. Sun, H. Liu, Y. Zheng
Key Laboratory of Optoelectronic Chemical Materials and Devices
Ministry of Education, Jianghan University
Wuhan 430056, P. R. China
E-mail: zhengyun@jhun.edu.cn
[d] Y. Zhao
China Institute of Ocean Engineering (Tsing Tao)
Qingdao 266555, P. R. China
[e] Dr. X. Rui
School of Materials and Energy
Guangdong University of Technology
Guangzhou 510006, P. R. China
E-mail: xhrui@gdut.edu.cn

Special Collection An invited contribution to a Special Collection on IV Symposium on Advanced Energy Storage.

Review
doi.org/10.1002/batt.202200481
Chemistry Europe
European Chemical Societies Publishing

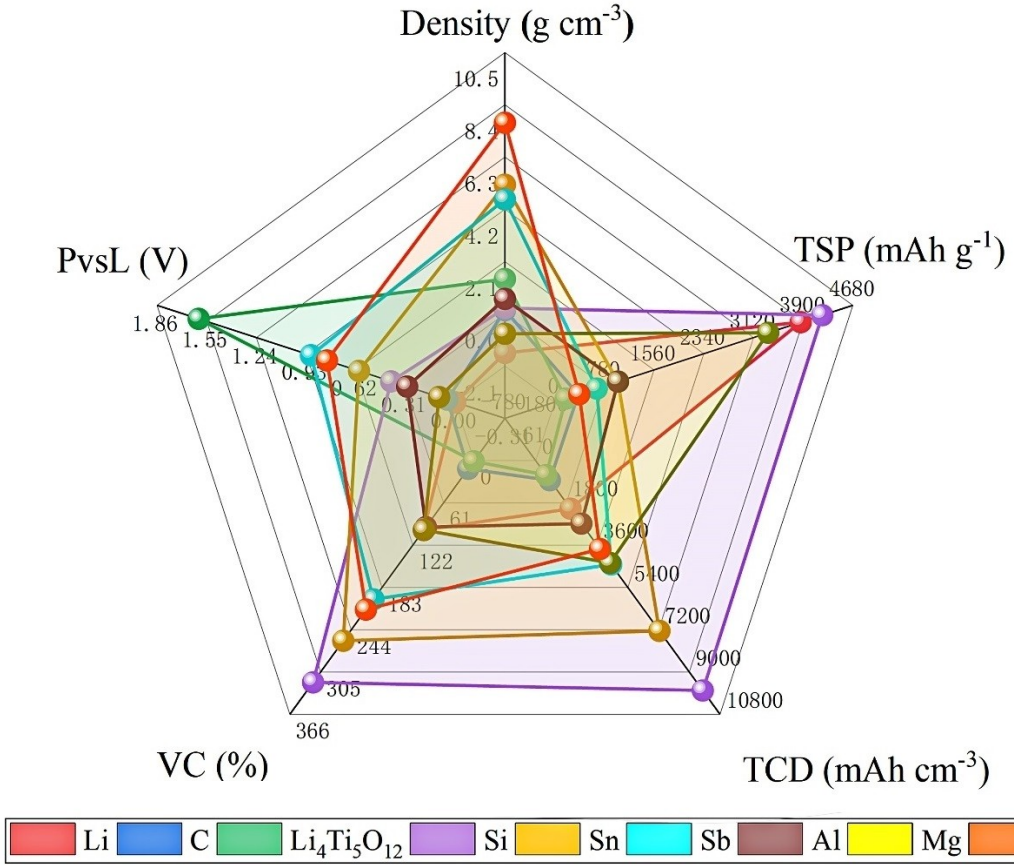

Figure 1. Performance comparison of common anode materials for LIBs in terms of theoretical specific capacity (TSP), theoretical charge density (TCD), volume change (VC), and potential vs. Li (PvsL).

Penglun Zheng is currently working at the Civil Aviation Flight University of China as an associate professor. He received his Ph.D. degree in Materials Science and Engineering in 2018 from the University of Electronic Science and Technology of China. In 2016–2017, he worked as a visiting scholar at Nanyang Technological University in Singapore. His research interests include flame retardants, lithium-ion batteries, and electrocatalysts.

Jichang Sun is currently a master candidate under the supervision of assoc. Prof. Penglun Zheng at the College of Civil Aviation Safety Engineering in Civil Aviation Flight University of China. His research interests focus on the key materials of lithium batteries.

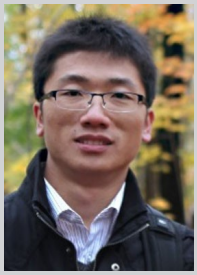

Yun Zheng is an associate Professor at Jianghan University, China. He received his BSc degree in Materials Physics in 2010 and Ph.D. degree in New Energy Materials in 2015 from the Wuhan University of Technology in China. During 2016–2019, he worked as a research fellow at Nanyang Technological University and the Institute of Materials Research and Engineering (IMRE) of the Agency for Science, Technology and Research (A*STAR) in Singapore. His research interests include thermoelectric materials and lithium-ion batteries.

Xianhong Rui is a professor at Guangdong University of Technology, China. He received his B.S. degree from the University of Jinan in 2007 and his M.S. degree from the University of Science and Technology of China in 2010. He then obtained his Ph.D. degree from the School of Materials Science and Engineering at Nanyang Technological University in 2014. His research interests mainly focus on the design and fabrication of advanced electrode materials for energy conversion and storage.

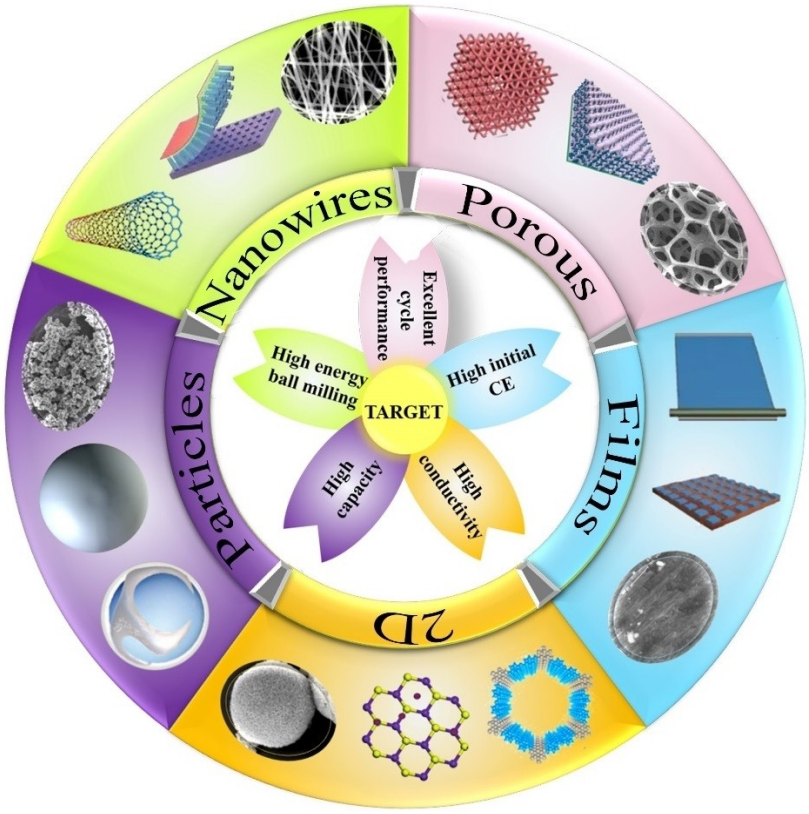

Figure 2. Schematic diagram of synthesis methods and alloy structures for silicon-based alloy anodes.

2. Synthesis of Silicon-based Alloys

High energy ball milling (HEBM)[29,30] is one of the most common methods for silicon alloy preparation because of its simple operation and energy efficiency. With the advancing technology, promising methods have been devised for the synthesis of silicon-based alloys, such as magnetron sputtering (MS),[31,32] pulsed laser deposition (PLD),[33,34] and electron beam evaporation (EBE).[35] The chemical methods include chemical vapor deposition (CVD),[36,37] electrostatic spray deposition (ESD),[38] and spin-coating technique.[39,40] In this section, the common methods for silicon-based alloy synthesis are introduced. Their principles, benefits and limitations are explained in detail.

2.1. High-energy ball milling

The question regarding "which method can allocate energy to chemical processes as effectively as possible?" remains an essential issue in the chemical research. HEBM, also known as a mechanochemical process, is a potential solution to the above concern.[41] HEBM involves the mixing process of materials as well as the following complex processes, i.e., automatic activation of solids, mechanical alloying, and corresponsive ball milling of solids.[42–44] The HEBM process flow is shown in Figure 3(a).[45] HEBM can significantly reduce the reaction activation energy, refine grains, enhancing powder activity, and promoting uniform particle distribution.[46–48] It has been widely used to obtain powder-form nanostructured materials with size of <100 nm.[49] These advantages empower HEBM-produced materials with excellent electrochemical properties for rechargeable batteries. For example, Wang et al. prepared NiSi nanocrystalline alloys using HEBM.[50] The SEM morphologies of NiSi alloy powders are shown in Figure 3(b). The NiSi anode shows a lithium storage capacity of 1180 mAh g^{-1} in the first discharge process. Furthermore, Park and coworkers conducted HEBM using Si, Ni, and graphite as raw materials.[51] Evidence of Si–Ni alloy formation and chemical bonding between alloy and graphite was claimed after the milling process. It also proved that HEBM is a facile process for physical blending and chemical bond formation. The ball milling time is one of the most important variables for achieving alloy materials. Lee et al. investigated the effect of ball milling time on the electrochemical properties of Ti–Si alloys.[52] This finding revealed that short milling time is insufficient to obtain alloy compounds, and long-time milling reduces the reversible capacity of alloy anodes. Recently, researchers have developed high-performance alloys by combining HEBM with other methods. For instance, Sun et al. adopted HEBM and a subsequent acid etching process to prepare porous SiAl alloys.[53] Their electrochemical properties can be optimized effectively by controlling porous silicon's porosity and size distribution in SiAl alloys. But problems also exist concerning the HEBM process, such as

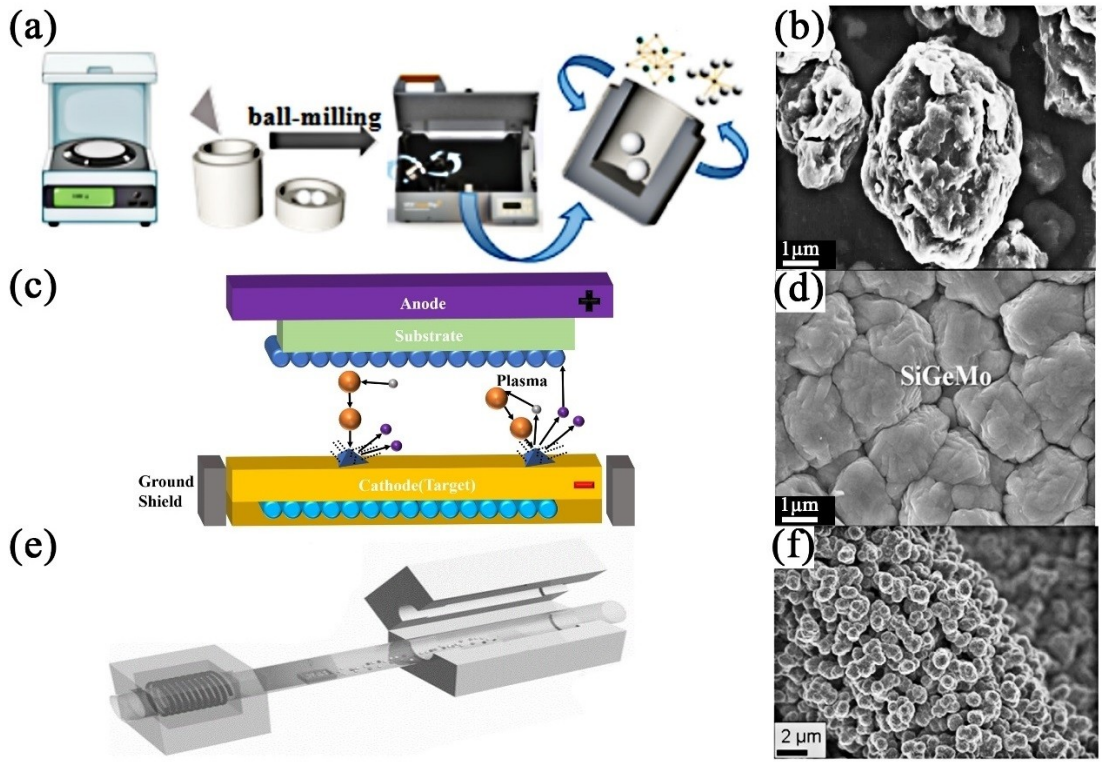

Figure 3. a) Schematic diagram of HEBM. Reproduced with permission from Ref. [45]. Copyright (2020) Elsevier. b) SEM micrograph of ball-milled NiSi alloy powders. Reproduced with permission from Ref. [50]. Copyright (2000) Elsevier. c) Schematic illustration of magnetron sputtering deposition. d) Overview of coated fibers of carbon-silicon-composites. Reproduced with permission from Ref. [54]. Copyright (2011) Elsevier. e) Schematic diagram of chemical vapor deposition. Reproduced with permission from Ref. [55]. Copyright (2017) Elsevier. f) SEM image of deposited silicon particles of carbon-silicon-composites. Reproduced with permission from Ref. [56]. Copyright (2008) Elsevier.

uneven size distribution of milled products, possible inclusion of impurities during the milling process, and an inert atmosphere required.

2.2. Magnetron sputtering deposition

The development of advanced coating deposition technology, especially physical vapor deposition (PVD), is relatively mature. The PVD process can be divided into sputtering and evaporation. Compared to sputtering, evaporation requires harsher and more directional environment, and the particle transfer has a higher quality (for larger particles) and a higher deposition rate.[57–59] The evaporation process is suitable for depositing thick films, where surface morphology is not the main concern. The sputtering process is appropriate for growing thin films. Magnetron sputtering (MS) technology is a more prominent representative. It involves transferring material from a target onto the substrate surface through a succession of incident ion impacts. The MS process is schematically displayed in Figure 3(c).[60] It has a large film-forming rate, low substrate temperature, good film adhesion, and large-area coating capability. The deposited (alloy) film has a smooth surface, outstanding mechanical energy, and friction performance and can maintain excellent adhesion with the substrate.[61] Many parameters are involved in the MS process, such as the number of vacuum pumps, gas type and flow, temperature, pressure, current density, bias, number of targets, and deposition process.[62] Refinement of these conditions allows the exploration of suitable thin-films.

Jiang et al. studied the influence of increasing N_2/Ar flow velocity on the microstructure evolution and mechanical responses of the grown AlSiN coatings.[63] Results indicated enhanced hardness for the AlSiN films with the increasing N_2/Ar velocity. Moreover, the MS technique was utilized to prepare Si-Ge-Mo films with optimized roughness, and thereby good cycle performance and high energy density (Figure 3d).[54] Recently, Zhang et al. prepared micron-scaled Si@Cu composite anodes by MS.[64] The results show that the as-prepared micron-sized Si particles can reduce the aggregation effect and improve the cyclic life of Si@Cu anodes. However, the generated plasma is unstable due to the low output rate of target materials (usually $< 40\,\%$).[65] This method also introduces impurities and has difficulty in controlling morphologies.

2.3. Chemical vapor deposition

Chemical vapor deposition (CVD) technology can control film composition and morphology by changing gas composition and pressure.[66,67] It uses various energy sources, such as heat, plasma excitation, or light radiation to produce gaseous/vapor

phases, which subsequently deposit on the required substrate (as schematically shown in Figure 3e). The CVD technology is suitable for low-cost synthesis, producing uniform and conformal layers, and preparing large-area films. It can be used for the preparation and modification of carbon-coated SiFe alloy films, which show enhanced cycle performance compared to the pristine SiFe films.[68] Wolf et al. adopted a modified CVD method to prepare nanocomposite anodes by depositing nanocrystalline and amorphous silicon on a carbon fiber matrix.[56] Figure 3(f) shows the SEM image of the as-prepared material. The carbon fiber serves as an "electron conductive network" and exhibits excellent adhesion to deposited silicon, demonstrating improved cycle performance, but the general limitations of CVD lie in its relatively low production rate, requirement of substrates, and complex preparation parameters, collectively resulting in the difficulty of large-scale production.[69]

2.4. Other methods

Electro-deoxidation uses oxides as raw materials to obtain metals and alloys via one-step electrolysis. It shortens the process flow and significantly reduces energy consumption and environmental pollution. Meanwhile, considering the facile control of compositions (via raw materials) and reduction degree (via electrolytic voltage and time) of oxides, it is suitable for preparing functional materials.[70–72] For instance, manganese silicon alloy powders were successfully prepared by electro-deoxidation.[73] Jiao et al. prepared intermetallic TiSi alloys by electro-deoxidation in molten $CaCl_2$ at 900 °C.[74] Moreover, Si/$TiSi_2$ heteronanostructures prepared by electrolysis show promising Li-storage performance when used as LIB anodes.[73,75] At a charge/discharge rate of up to 8400 mA g^{-1}, the Si/$TiSi_2$ anodes show a specific capacity of >1000 mAh g^{-1} and a slight capacity attenuation of 0.1% per cycle during 20th–100th cycles. The electro-deoxidation method shows main limitations in preparing high-purity (>99%) materials and production rates.[76]

In addition, other methods have been applied to prepare Si-based alloy anodes, such as electrostatic spray deposition (ESD),[77] sol-gel method,[78] and electrospinning.[79,80] Despite the various preparation methods for silicon-based alloys, they have their benefits and limitations. The selection or combination of appropriate preparation methods is significant for the production of Si-based alloys with promising properties.

3. Advances in Silicon-based Alloy Anodes

Si-based alloys have the advantages of maintaining the superior specific capacity of silicon and high initial Coulombic efficiency, as well as inhibiting volume changes to a certain extent.[20,70] In recent years, researchers have focused on developing silicon-based alloy anodes with multi-dimensional structures, such as nanowire structure,[81,82] porous structures,[83–85] and films.[86–88] For example, SiGe alloys with different morphologies possess considerably different performances. SiGe alloys with 3D porous nanostructures demonstrate a reversible capacity of 1311 mAh g^{-1} after 45 cycles at 4 A g^{-1}.[84] Stokes et al. prepared SiGe alloy anodes with nanowire arrays through an electrospinning technology. Under a constant current at C/5 (1 C = 1000 mA g^{-1}), the capacity of 1360 mAh g^{-1} was retained after 250 cycles.[82] Despite many studies on Si anodes with multi-dimensional morphologies, few types of research focus on their alloys. Therefore, it is critical to reveal the influence of silicon alloys with various microstructures on the LIB performance (as shown in Table 1). It can be concluded that morphologies significantly impact the electrochemical properties of Si alloy anodes. This section will review the recent progress on microstructure engineered Si alloy anodes for LIBs.

3.1. Si-based alloy nanoparticles

Researchers tend to combine morphology control and alloying impact to improve the electrochemical properties of silicon-based anodes, among which silicon alloy nanoparticles are the most frequently studied.[100] Wang et al. prepared electrodes with micron- and nano-silicon particles and studied their effects on the LIB performance.[101] Nano-silicon anodes possess larger

Table 1. Comparison of properties of different silicon-based alloy materials.

Si alloy	Current density [mA g^{-1}]	Initial CE	Specific capacity [mAh g^{-1}]	Synthesis method	Structure	Cycle Number	Ref.
$Ni_{0.2}Si_{0.8}$	200	70.00%	1617	HEBM	Nanoparticles	50	[89]
$Ti_{0.85}Si_{0.15}$	200	81.00%	1372	HEBM	Nanoparticles	50	[90]
$Fe_{14}Si_{86}$	100	92.00%	1192	HEBM	Nanoparticles	100	[91]
$ZnSiP_2$	200	99.50%	1789	HEBM	Nanoparticles	500	[92]
$Si_{0.67}Ge_{0.33}$	200	95.00%	1360	CVD	Nanowires	250	[82]
Type-G SiGe	100	70.50%	1266	VLS	Nanowires	400	[93]
Si/$TiFeSi_2$	200	80.00%	1100	Arc-Melting	Two-dimensional	100	[94]
Si/Ni_3Si	100	72.50%	1132.4	Electrospinning	Two-dimensional	200	[95]
$Si_{12}Ge_8$	1000	75.60%	1158	Dealloying	Porous	150	[85]
(NP)Si/Zn	1000	88.90%	901.8	Dealloying	Porous	1000	[96]
$Si_{0.75}Ge_{0.25}$	100	79.90%	2121	GLAD	Films	50	[97]
SiGe@Cu	200	99.20%	1567	MS	Films	80	[98]
Mg_2Si	380	99.99%	960	MS	Films	400	[99]

specific capacity and better capacity retention than micron-silicon. In addition, silicon anodes with nanosized particles have good relaxation and strain capabilities that can reduce the mechanical fracture and dramatically improves LIB's safety.[102] The above benefits originate from the large specific surface areas of nano silicon and the enhanced contact areas between these active particles.[103] Nickel (Ni) is a cost-effective metal with good electrical conductivity. Due to its good adhesion with Si, it can be well combined with Si to form Si–Ni alloys.[104] NiSi alloy particles with an average size of 4–6 nm were prepared through HEBM.[89] The as-synthesized NiSi nanoparticles exhibit improved electrochemical properties. Furthermore, Du and coworkers systematically investigated ball milling time and constituents on the phase composition of NiSi alloys.[90] The Ni–Si alloys (Ni_xSi_{1-x}, $0 \le x \le 0.5$) with different Si and Ni components were studied as LIB anodes. XRD patterns of Ni_xSi_{1-x} alloys after ball milling are shown in Figure 4(a). At $x \le 0.25$, the nanostructured Si/$NiSi_2$ alloy was obtained, and NiSi appears gradually with further increasing x. Figure 4(b) compares the volumetric specific capacities and volume expansion of these composition-dependent alloys. Figure 4(c) shows the cycling performance of these NiSi alloy anodes. Evidently, Ni_xSi_{1-x} ($0 \le x \le 0.5$, $\Delta x = 0.05$) alloys present improved cycling stability over the pristine Si anode due to the effective elimination of the cycling-induced $Li_{15}Si_4$ formation. Afterward, Wang et al. combined Ti with Si to achieve Ti–Si alloys because of the good conductivity, low density, and advanced thermal and chemical stability for Ti.[105,106] Ti_xSi_{1-x} ($0 \le x \le 0.3$, $\Delta x = 0.05$) alloys prepared by ball milling demonstrate decreased volume capacities and volume expansion with the increasing Ti content, as shown in Figure 4(d).[107] This can be attributed to the suppression of generated $Li_{15}Si_4$ phase with the $TiSi_2$ introduction.

Another issue concerning the commercialization of anode materials is the material cost. Iron is the most common metal element in many fields because of its low cost and rich resources.[108] For the Si-based alloy anode, the iron addition endows Fe–Si alloys with fast electron transfer.[109] More importantly, Fe–Si alloy can ensure the mechanical integrity of the silicon-based anodes.[110] Generally, Fe–Si alloy consists of Si

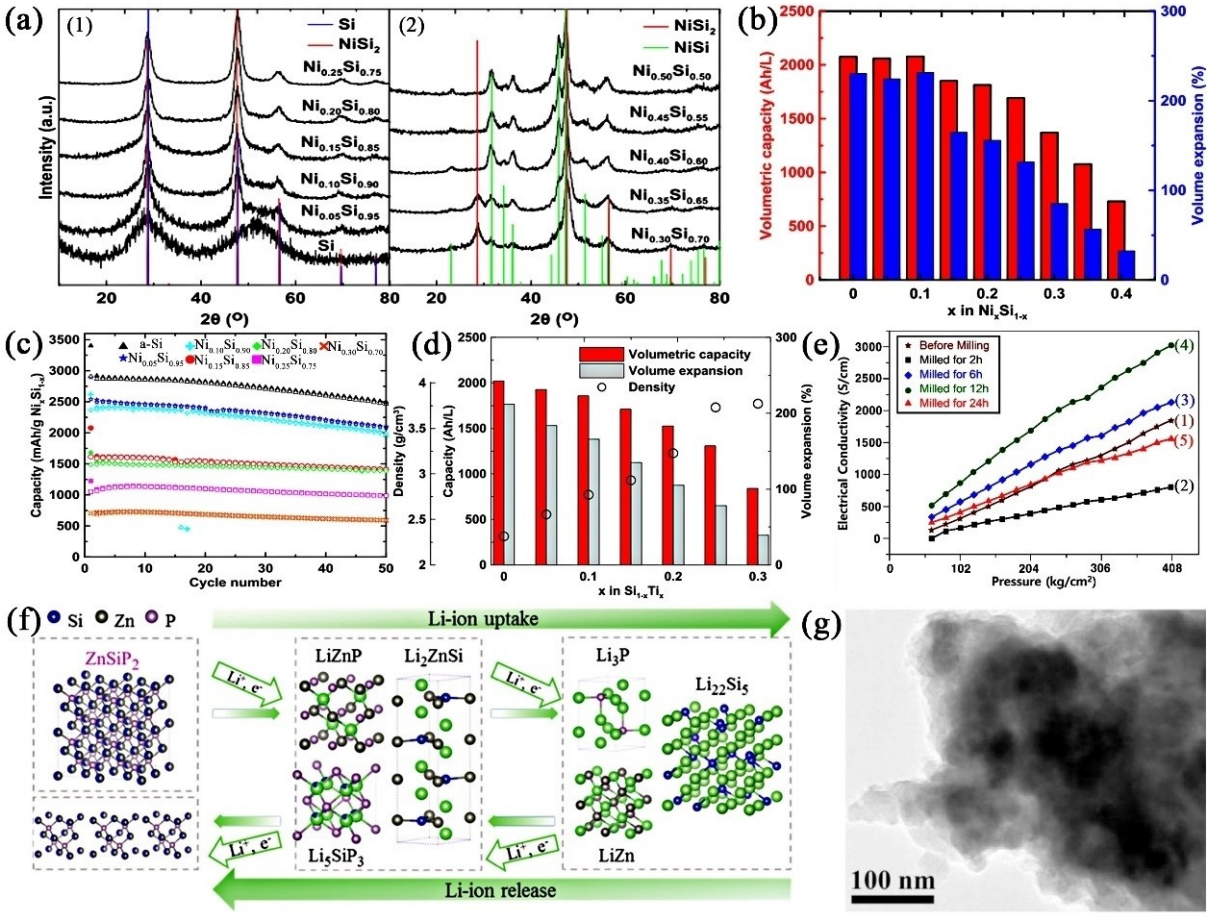

Figure 4. a) XRD patterns of Ni_xSi_{1-x} alloys: (1) $0 \le x \le 0.25$; (2) $0.30 \le x \le 0.50$. b) Composition dependent volumetric capacity and volume expansion of Ni_xSi_{1-x} alloy. c) Cyclic performance of Ni_xSi_{1-x} alloys. Reproduced from Ref. [90]. Copyright (2015) The Author(s). Published by ECS. d) Relationship between density, volume capacity, and volume expansion of $Si_{1-x}Ti_x$ ($0 \le x \le 0.3$) alloys. Reproduced from Ref. [107]. Copyright (2017) The Author(s). Published by ECS. e) Compression pressure dependent electrical conductivity of Fe–Si alloys before milling and after milling for 2–24 h. f) The illustrated Li-storage mechanism of $ZnSiP_2$ anode. g) High-resolution TEM (HRTEM) image of the cation-disordered $ZnSiP_2$/graphite composite. Reproduced with permission from Ref. [92]. Copyright (2008) Royal Society of Chemistry.

and $FeSi_2$. The inert $FeSi_2$ is usually adopted as a buffering matrix to accommodate the volume expansion of silicon-based anodes, thereby suppressing morphological degradation.[91] Ruttert et al. prepared Fe_xSi_y alloys using HEBM, and studied the structural stability and cycle performance of FeSi alloy anodes.[109] Results indicate that Fe_xSi_y alloys anodes without additional prelithiation exhibit high area capacity, high initial Coulombic efficiency (ICE) and stable cycle performance. Although FeSi alloy anodes demonstrate partially improved capacity retention over Si anodes, their capacities need to be improved further to accommodate practical applications. Furthermore, Fe–Si alloy/carbon (denoted as Fe–Si/C) nanocomposites were prepared using sand grinding.[91] The Fe–Si/C anode materials show a highly reversible capacity and long-cycling stability. Lee et al. extended the HEBM time up to 24 hours and achieved structurally stable Fe–Si alloys by reducing the silicon size and forming the α-$FeSi_2$ phase.[111] The effect of milling time on the alloy morphologies and their corresponding electrochemical performance were analyzed. Electrical conductivities of the Fe–Si alloys as a function of compression pressure are shown in Figure 4(e). On account of the high durability and enhanced electrical conductivity of β-$FeSi_2$, the Fe–Si alloys milled for 12 hours demonstrated the best battery performance.

The above binary silicon alloys demonstrate considerable improvements in electrochemical performance compared to pristine silicon anode. But researchers explored ternary silicon-based anodes aiming to further improve their specific capacities and cycling performance.[112,113] The thermodynamic stability of ternary compounds is limited, requiring good design, appropriate chemical composition analysis, and proper working potential selection.[114] A fundamental understanding of the composition-structure-performance relationship is key to developing new battery technology.[115,116] The successful design of ternary Si alloy anodes generally results in promising electrochemical performance. For example, a new cationic disordered Zn–Si–P with sphalerite structure was successfully synthesized via HEBM using the corresponding powder elements as raw materials.[92] As illustrated in Figure 4(f), the $ZnSiP_2$ anode shows excellent Li-storage capability because of its fast electron/Li^+ diffusion and improved tolerance to volume change. After further mixing with carbon (the morphology is shown in Figure 4g), the $ZnSiP_2$@C composite anode demonstrated specific capacities of 1789 mAh g^{-1} at 200 mA g^{-1} (after 500 cycles) and 585 mAh g^{-1} at 30 A g^{-1}. The excellent lithium storage properties are attributed to their superior structural reversibility, fast Li^+/electron transfer, and unique Li-storage mechanism.

3.2. Si-based alloy nanowires

Silicon nanowires can also effectively alleviate the pulverization of silicon anodes and favor electron transport due to the unique one-dimensional structure.[117] Many preparation methods can be adopted to obtain silicon-based alloy nanowires. They can be roughly divided into the growth method and the etching method.[118] Stokes et al. utilized the growth method to explore the feasibility of growing silicon alloy nanowires.[82] The $Si_{1-x}Ge_x$ alloy nanowire array was grown directly on the current collector as schematically illustrated in Figure 5(a). Compared to Si, $Si_{1-x}Ge_x$ alloy nanowires show higher capacity retention and cycle performance because of their higher lithium diffusion rate and more advanced electrical conductivity at room temperature (Figure 5b).[119,120] The high-resolution SEM image in Figure 5(c) shows the detailed nanowire morphology. The preparation of these $Si_{1-x}Ge_x$ ($0.33 \leq x \leq 0.80$) nanowires stands for a facile and efficient synthesis method which combines the benefits of both Si (large capacity) and Ge (high-rate performance and good capacity retention). The $Si_{0.67}Ge_{0.33}$ anode presents the best cycling performance, sustaining a discharge capacity of 1364 mAh g^{-1} after 250 cycles at 200 mA g^{-1}.[82] This work indicates the feasibility of synthesizing Si-based alloy nanowires, offering creative and alternative options for researchers to achieve optimized silicon-based anodes for LIBs.

Kim et al. used the vapor-liquid-solid (VLS) method to control the atomic arrangement in the SiGe alloy anode materials with significantly improved structural stability, as shown in Figure 5(d).[93] Its principle is to use surface segregation (enrichment of a component on the surface of binary alloy) to achieve fine control of the overvoltage. Both of G-type and U-type SiGe nanowires show good electrochemical properties. Nevertheless, the G-type nanowires show higher reversible capacity ($>$1031 mAh g^{-1}) and longer cycle life (400 cycles), and higher capacity maintenance (89.0%) at 0.2 C (1 C = 1200 mA g^{-1}). This excellent battery performance is attributed to the fact that the G-type SiGe NWS (850 °C) uses the unphysical and chemical parts as the support frame, thus effectively preventing the crushing of related anode materials. This work suggests that the rearrangement of silicon atoms may alleviate the serious changes of anode morphology.

Furthermore, copper, a ductile, highly conductive, and low-cost element, was involved to obtain SiCu alloy anodes with nano-columnar structures by ion-assisted oblique angle co-deposition technique.[81] The diagram is shown in Figure 5(g). Cu significantly reduces the total capacity loss and realizes fast electron transfer.[121] The SiCu alloys show stable cycling performance (Figure 5h). The influence of the silicon to copper ratio on the electrode morphology was investigated. The cross-sectional SEM image is shown in Figure 5(i). The increasing surface Cu content in the anodes can minimize the crack formation and film delamination, but the alloy anodes present slightly decreased capacities.

3.3. Two-dimensional Si-based alloys nanostructures

Two-dimensional (2D)[122] materials have many advantages: 1) the atomic sheets of 2D materials offer abundant sites for active electrochemical reactions; 2) vacancy defects formed by the atoms escaping from the lattice, reducing the coordination number of particles on the surface of 2D materials.[123] The vacancy formation can change the crystal morphology. Moreover, the bandgap can be adjusted by atomic motion.[124–126]

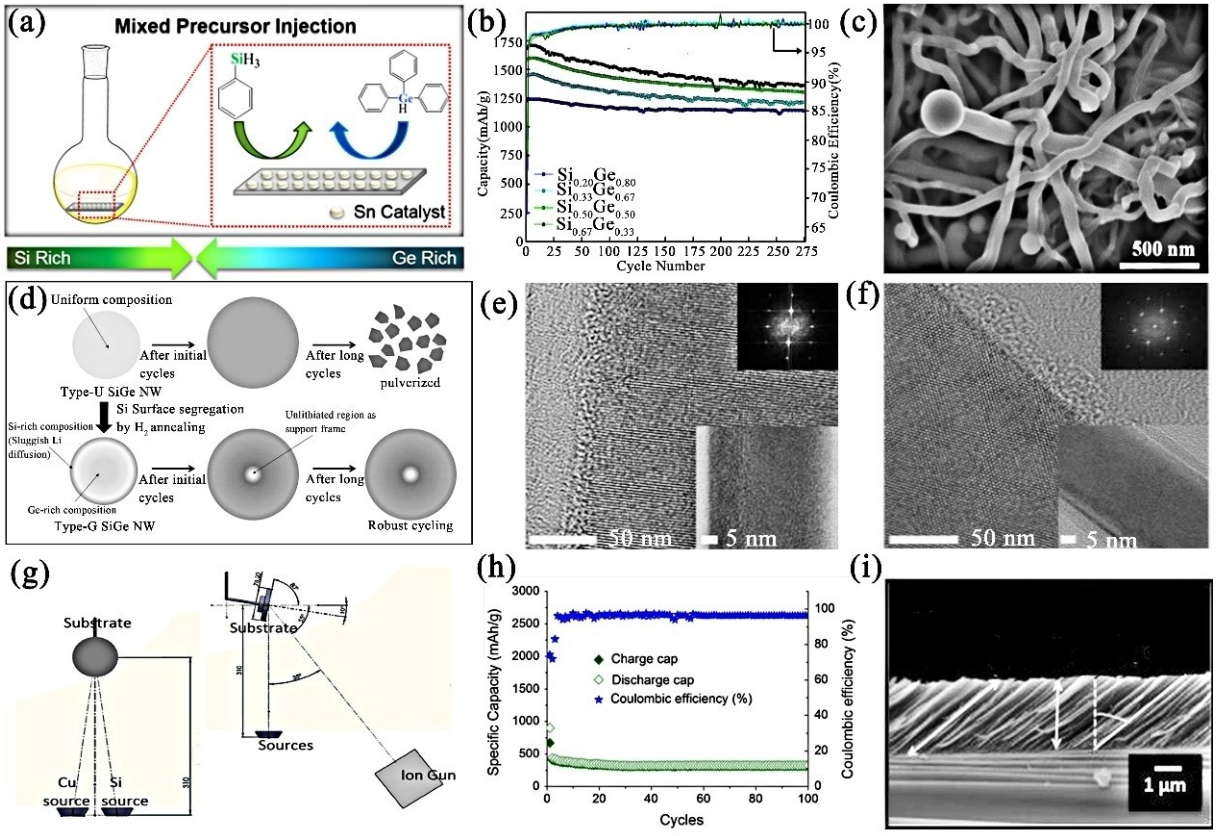

Figure 5. a) Schematic diagram for the synthesis of $Si_{1-x}Ge_x$ alloy nanowires. b) Cycling performance and Coulombic efficiencies for $Si_{1-x}Ge_x$ alloy nanowires. c) Morphologies of $Si_{0.67}Ge_{0.33}$ nanowires. Reproduced with permission from Ref. [82]. Copyright (2017) American Chemical Society. d) Schematic illustration of a novel SiGe anode design. Representative HRTEM images of e) type-U SiGe nanowires and f) type-G SiGe nanowires. Reproduced with permission from Ref. [93]. Copyright (2015) American Chemical Society. g) Schematic representation of the experimental setup for oblique angle deposition. h) Discharge capacities as functions of cycling number. Reproduced with permission from Ref. [81]. Copyright (2016) Springer Nature. i) SEM cross-sectional image of 30 at% Cu. Reproduced with permission from Ref. [81]. Copyright (2016) Springer Nature.

3) Ions and electrons can transfer rapidly in the layered structures without obvious interruption.[127,128] Researchers have recently explored a 2D arrangement of silicon alloy with good conductivity and reduced volume expansion for LIB applications.

Based on the previous research, Park et al. found that introducing a small amount of Ti and Fe into Si (via melt spinning) can improve the Si anode's performance.[94] They proved that the electrochemical property of active and inactive $Si/TiFeSi_2$ nanocomposite anodes can be further improved by microstructure modification (via HEBM), as shown in Figure 6(a). The $Si/TiFeSi_2$ nanocomposite electrode shows an invertible capacity of ~1000 mAh g^{-1}, an ICE of ~80%, and good rate performance. XRD analysis combined with electron microscope observation showed that $Si/TiFeSi_2$ nanocomposite microstructure was successfully regulated by HEBM-induced mechanical deformation (Figure 6b). Despite the same composition of $Si/TiFeSi_2$ nanocomposites before and after HEBM, the corresponding phases (in the final lithiation stage) and electrochemical properties of electrodes are different and highly dependent on their microstructure. The mechanical grinding results in the size reduction of Si and $TiFeSi_2$ and formation of homogeneous nanocomposites. The Si phases with several nanometers in size are finely dispersed in $TiFeSi_2$, as schematically shown in Figure 6c.

The density functional theory (DFT) calculation is effective for revealing the electronic structure of multi-electron systems, understanding the electrochemical reaction mechanism, and screening promising energy storage materials.[131] DFT was utilized to study the electronic structure of Cu_2Si monolayers, and the adsorption/distraction of Li on Cu_2Si monolayers.[129] The calculation results prove that Cu_2Si monolayers are expected anode materials for Na-ion batteries. To further explore the storage mechanism of Cu_2Si monolayer, the adsorption configuration of Li on Cu_2Si monolayers was studied (Figure 6d). The calculated adsorption energies for Li on the possible adsorption sites are displayed in Figure 6(e). Recently, the first-principle DFT was applied to investigate the possibility of using a monocyclic aromatic hydrocarbon-derived structure (Figure 6f) as the LIB anode.[130] This 2D structure resembles monoene or graphene; the moiety of the tin atoms are substituted by Si to form a novel Sn–Si alloy. The calculation results show that the optimized structure can improve the anode performance. Further computation of the Li adsorption

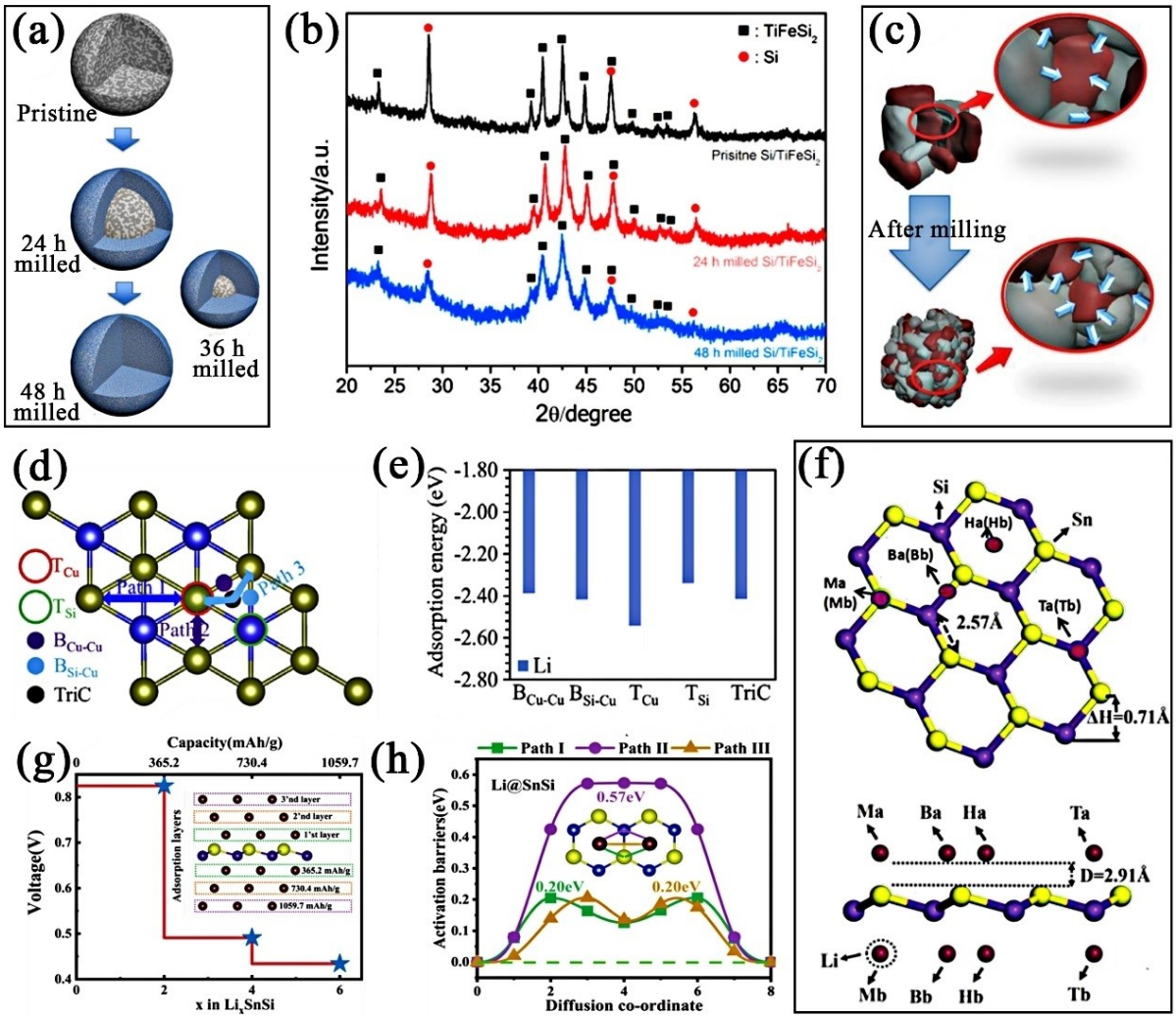

Figure 6. a) Schematic illustration of microstructure evolution with respect to milling time. b) XRD patterns of Si/$TiFeSi_2$ nanocomposites. c) Refining size of active Si and inactive $TiFeSi_2$ matrix prepared by mechanical milling. Reproduced with permission from Ref. [94]. Copyright (2016) Elsevier. d) The lithium adsorption sites. e) The adsorption energies of lithium on Cu_2Si. Reproduced with permission from Ref. [129]. Copyright (2019) Elsevier. f) SnSi monocyclic aromatic hydrocarbon derived structure. g) The voltage profiles and storage theoretical capacities of Sn–Si. h) Diffusion barrier and the corresponding pathways of Li on Sn–Si monolayers. Reproduced with permission from Ref. [130]. Copyright (2021) Royal Society of Chemistry.

content on Sn–Si alloy monolayers confirms that this material can meet the requirements of battery anode in open-circuit voltage and storage capacity (Figure 6g). The diffusion path of a single lithium-ion on the Sn–Si monolayer surface was calculated taking advantage of the climbing image nudged elastic band (CL-NEB) method (Figure 6h). Three representative paths are considered for calculation from the diffusion barrier diagram of the Sn–Si/Ge monolayer, as shown in Figure 6(h). The path I–III follow the monolayer surface. These low voltage values indicate that the Sn–Si monolayer is a promising LIB anode (with a theoretical capacity of ~1096 mAh g^{-1}).

3.4. Porous Si-based alloys

Volume expansion of electrodes results in declined capacity after a certain number of charge/discharge cycles, especially at high current rates.[1] Porous silicon design can solve the serious volume expansion in the pristine silicon anode. The synthesis of porous silicon can be divided into top-down and bottom-up methods. The top-down means generally use simple techniques, including chemical and electrochemical corrosion. In contrast, the bottom-up approach usually requires a porous template.[132] On the one hand, porous structures can alleviate the cycling-induced stress and strain and retain the electrode integrity without pulverization. On the other hand, the large surface areas originating from the porous morphology are conducive to rapid Li^+ diffusions from the electrolyte to the silicon-alloy anode, thus improving the high-rate charge/discharge capacity and cycling stability.[133,134] Numerous research has concentrated on the porous structure of pristine Si anodes, but few studies relative to porous Si alloy anodes have been reported. This section introduces the research on Si alloy

anode to understand the characteristics of porous Si alloy anodes.

Wang et al. prepared a 3D SiGe alloy electrode using a template-assisted method.[84] Figure 7(a) shows a typical SEM image of a nanoporous copper collector with an ordered pore structure (pore size ~200 nm). Figure 7(b) shows a SEM image of SiGe alloy supported on a nanoporous copper collector with 30 min sputtering time. Results show that the SiGe alloy presents a uniformly distributed ordered porous structure. The LIB electrode reveals a reversible capacity of 1311 mAh g^{-1} after 45 cycles at 4 A g^{-1}. The anode can deliver a stable capacity of ~1047 mAh g^{-1} at a current density of up to 16 A g^{-1}. The porous structures effectually moderate the volume extension during cycling. They also provide large contact areas between SiGe alloy and Cu collector to improve the conductivity of SiGe.

Although the above-mentioned nanoporous SiGe alloy anode shows stunning performance, its preparation is relatively complex and time-consuming, and the composition of SiGe alloy has not been clarified. Furthermore, Yang et al. prepared a 3D nanoporous (3D-NP) SiGe alloy by a simple dealloying

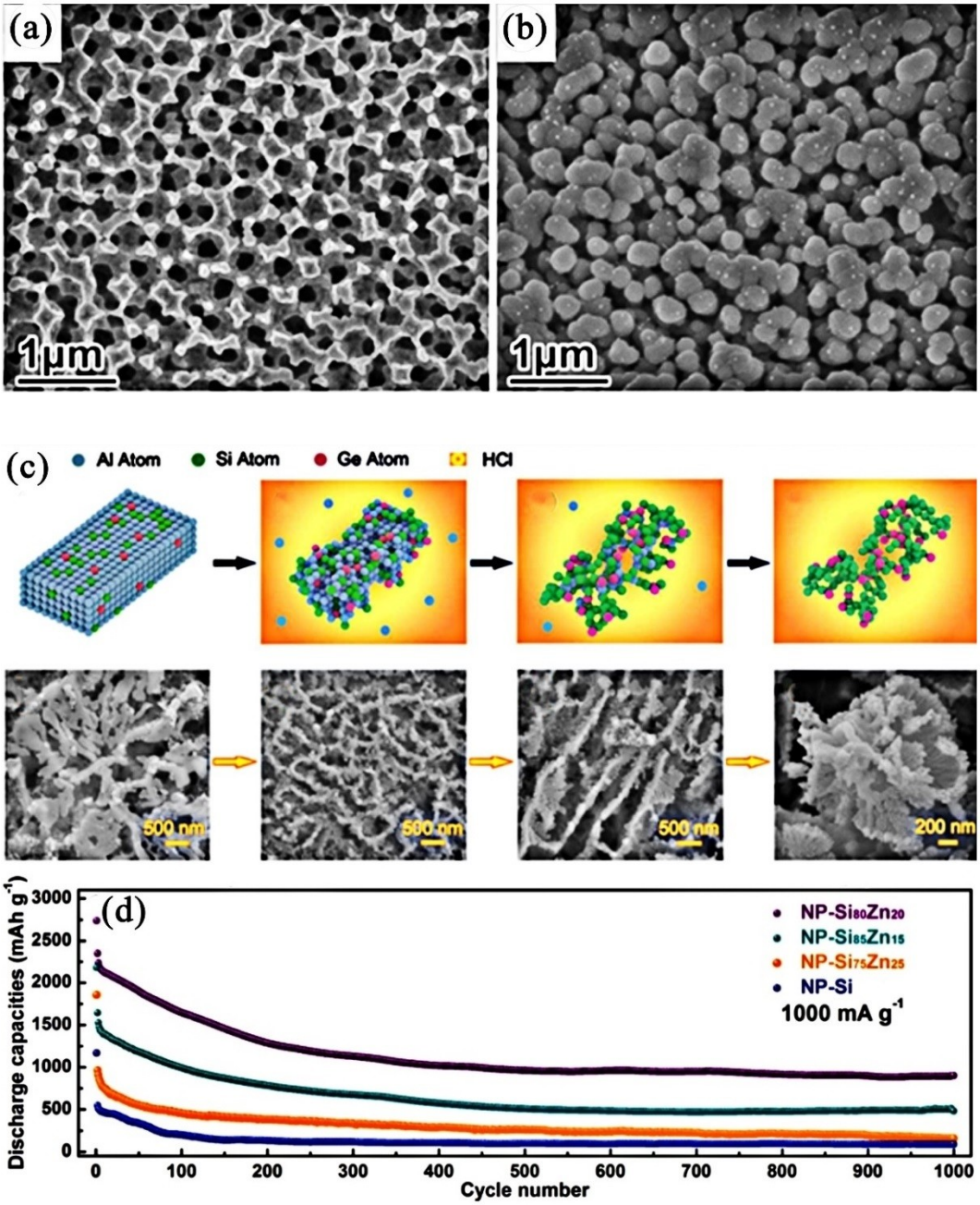

Figure 7. a) SEM morphology of the nanoporous Cu current collector; b) Top-view of the porous current collector deposited with SiGe alloys. Reproduced with permission from Ref. [84]. Copyright (2013) Elsevier. c) Schematic of the evolution of 3D-NP SiGe structure. Reproduced with permission from Ref. [85]. Copyright (2018) American Chemical Society. d) Cycling performances of NP–Si/Zn composites and NP–Si under a high current density of 1000 mA g^{-1}. Reproduced with permission from Ref. [96]. Copyright (2018) Elsevier.

method.[85] Al was incorporated as an excess material, Si and Ge were used as connecting material, and HCl was used as a dealloying medium to prepare the Al_{100-x}-$Si_{0.6x}$-$Ge_{0.4x}$-HCl ($x=10$, 15, 20, 25, 30) system (Figure 7c). 3D NP SiGe ($x=30$) demonstrates a uniform coralline morphology with hierarchical micropores and mesopores. The reversible capacity of the $Si_{12}Ge_8$ alloy ($x=20$) anode is 1158 mAh g^{-1} after 150 cycles at 1000 mA g^{-1}. Compared to Si negative electrodes, SiGe alloys present accelerated electron/Li^+ transfer due to their coral structures and the incorporation of Ge, resulting in good rate capability. Considering the lower conductivity and higher cost of Ge than Zn, Chen and coworkers utilized SiZnAl as the precursor to prepare a porous Si-based alloy.[96] Porous Si/Zn composites with controllable composition and large porosity were obtained through one-step operation and selective dealloying treatment. The as-synthesized Si/Zn composites demonstrated open interconnected 3D network and multi-scale pore distribution. The reversible capacity of the optimized nanoporous $Si_{80}Zn_{20}$ alloy is as high as 901.8 mAh g^{-1} after 1000 cycles at 1000 mA g^{-1} (Figure 7d). In addition, the full cell assembled with $LiFePO_4$ cathode and nanoporous $Si_{80}Zn_{20}$ anode shows an ICE of 88.9% and good cycle stability.

3.5. Si-based alloy films

The thin-film structure has also been studied extensively to address the following issues of silicon anodes, such as low electrical conductivity and severe volume expansion during cycling.[135] In general, the film thickness ranges from subnanometers to several microns. In contrast to other conventional types of LIB anodes, thin-film Si anodes show more consistent output voltage, smoother electrode quality, and longer cycle life.[136] The thin film structure has a large surface area to volume ratio, greatly enhancing the transfer of electrons and lithium ions due to the shortening transmission path.[137,138] This structure is also beneficial to accommodate the mechanical stress induced by Li-ion insertion/extraction. Furthermore, the thin film has an excellent geometric structure, and its chemical composition could be accurately detected and controlled. Currently, the thin-film anode has become a promising research direction.[139,140] The electrochemical properties of the obtained thin film anode largely depend on the nanosize effect and the chemical composition of the film.

The stoichiometric silicon carbide (SiC) component has recently been explored as an anode material for LIBs. Compared to the pure silicon, SiC films exhibit better capacity retention because it can serve as a robust buffering matrix to relieve the volume expansion of silicon during cycling (which signifies advanced mechanical stability).[141] Huang et al. explored SiC thin films by inductively-coupled-plasma chemical-vapor-deposition (ICP-CVD).[142] Figure 8(a) shows the cycle performances of Si and SiC at 0.3 C (1 C = 1000 mA g^{-1}). Despite a decreased initial capacity, the cycle stability of SiC anode has been greatly improved. Morphologies of the SiC and pristine Si anode before and after cycling tests are shown in Figure 8(b). Evidently, the Si electrode shows large cracks after cycling while SiC is relatively stable. Moreover, reducing the thickness of silicon carbide was proved effective in enhancing the specific

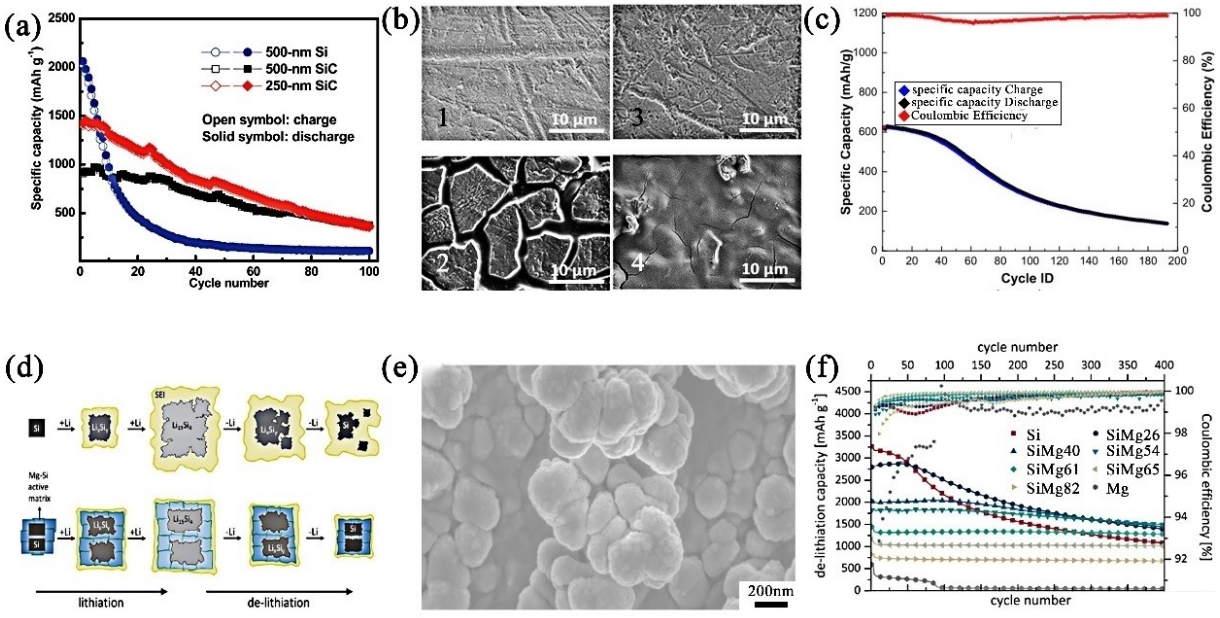

Figure 8. a) Cycle performance of SiC and Si anodes at a current density of 0.3 C. b) SEM images before cycling: (1) 500 nm Si and (3) 500 nm SiC; SEM images after cycling: (2) 500 nm Si and (4) 500 nm SiC. Reproduced with permission from Ref. [142]. Copyright (2018) The Royal Society of Chemistry. c) Cyclic stability of SiGe alloy at 2.5 C. Reproduced with permission from Ref. [143]. Copyright (2015) American Chemical Society. d) Schematic diagram of Li^+ removal of SiMg alloy. Reproduced with permission from Ref. [143]. Copyright (2015) American Chemical Society. e) SEM image of SiMg65. f) Coulombic efficiency and capacity curves of silicon films with different compositions. Reproduced with permission from Ref. [143]. Copyright (2015) American Chemical Society.

capacity but reducing the capacity retention. The SiC thin-film (500 nm in thickness) anode demonstrates good capacity.

SiGe alloys are considered as one of the simplest alloy types in LIBs, and their film structure is also outstanding. Si and Ge are group IV elements with similar Li^+ insertion/extraction behavior. Considering the high theoretical capacity, fast Li-ion diffusion, and considerable electrical conductivity of Ge, it can be alloyed with Si to enhance electrode materials' performance.[97] For instance, amorphous nanostructured SiGe alloy films were synthesized by glancing angle deposition (GLAD).[87] The capacity of the pure Si film is 2640 $mAh\,g^{-1}$, while that of Ge film is 1217 $mAh\,g^{-1}$. The SiGe alloy film demonstrates slightly lower capacity than the Si film but much higher than the Ge film. As shown in Figure 8(c), the cycle stability of SiGe film is improved. Silicon alloyed film reduces the cost of Ge and improves the cycling stability.

Mg can be reversibly (de)lithiated with Li^+, and alloying with Si can compensate for its defects, as schematically shown in Figure 8(d). Mg–Si thin films were produced by a RF magnetron sputter deposition in a customized Bestec sputter. Figure 8(e) shows the morphology of the synthesized Mg Si alloy. Figure 8(f) shows the performance of the Mg–Si alloy with different compositions after 400 cycles at a constant current.[143] Therefore, combining Si and Mg can greatly improve its cycle performance. However, compared with Si, the alloy anode's capacity still has room for further improvement, and its Coulombic efficiency remains low. The specific capacity of Al is 2235 $mAh\,g^{-1}$ (i.e., about six times graphite), and its electrical conductivity is very high. In addition, alumina oxide (Al_2O_3) is often used to improve silicon-based anodes' electrochemical performance and cycle stability. Jiang et al. continued to explore AlSi alloy, which showed an irreversible capacity of 1500 $mAh\,g^{-1}$ and an initial CE of 99.9% at 100 $mA\,g^{-1}$.[144] The AlSi film has a better rate and cyclic performance than pure Si film with the same thickness. It also can be inferred that the Li-ion diffusion coefficient of AlSi films ($2.38\times10^{-7}\ cm^2\,s^{-1}$) is two orders of magnitude larger than that of the pure Si film ($2.16\times10^{-9}\ cm^2\,s^{-1}$).

4. Conclusion and Perspective

Thanks to the low cost, high capacity, and many other advantages, Si-based alloys are considered ideal LIB anodes. However, the considerable volume expansion during cycling, inferior electrical conductivity, and incompatibility with electrolytes serve as the main obstacles to the further development and wide application of silicon-based anodes. Researchers have explored many solutions to address these problems by combining alloying and microstructure engineering.

This paper reviews the recent progress on microstructure-engineered Si-based alloys. Firstly, the common methods for the synthesis of silicon alloys are introduced, and the advantages/disadvantages of these synthesis methods are analyzed. This can help readers understand how to prepare Si-based alloys. Then, we summarize the research progress of silicon-based alloy anodes with various microstructures, including nanoparticles, nanowires, two-dimensional nanostructures, porous structures, and thin films. These different morphologies retain the high capacity of Si materials, but the unique morphology and structure can endow silicon-based alloys with diversified advantages. For example, porous structures can significantly alleviate the volume expansion of silicon-based anodes and improve electrical conductivity. These analyses can enable readers to clearly understand the impact of morphology on Si alloys.

In addition, Si-based anodes also have good prospects in sodium-ion batteries and solid-state lithium batteries,[145] and many researchers are also committed to this research. Zheng et al.[146] reviewed alloy anodes in sodium batteries, especially Si alloy anodes, and Song et al.[147] analyzed the advantages of Si alloy anodes in potassium batteries. However, silicon-based anode still has insufficiency to meet the commercialization requirements. For example, the HEBM method is the most popular for preparing Si-based alloy anodes, but its stability cannot be controlled by increasing the milling cycles and milling time; it is thus important to search for an efficient preparation method to realize the large-scale production of Si-based alloys.[148] Extensive efforts have been devoted to exploring the composition of Si alloy anode materials, but the conductivity and cyclic performance are boosted in a certain extent and the capacity is still relatively low.

Security of LIBs has always been the most important issue that people are concerned with. The volume change of silicon in the electrochemical reaction is as large as 300%, which is much larger than the 10% volume change of existing carbon materials.[149] Although the volume expansion of silicon-based alloy anodes has been alleviated, its safety cannot be fully guaranteed. Moreover, most microstructure-engineered silicon anodes have high surface areas that can result in severe side reactions with the electrolyte and thereby form unstable SEI films. The repetitive cycling induced volume expansion causes the crack of SEI films which contributes to the uneven lithium plating instead of alloying with silicon, thus resulting in the lithium dendrite formation. The growth of lithium dendrites will pierce the separator, leading to short circuits, liquid leakage, and even battery explosion.[150] Although there have been safety detection means of using ultrasonic sensing for data fusion analysis and building new battery health indicators to monitor the ultrasonic sensing technology of commercial lithium-ion pouch cells, it has not been widely used,[151] and its safety also needs to be further studied and explored. Safety standards and relevant tests have been developed to analyze battery performance and influencing factors to meet the required safety requirements. Among them, the GB/T 31485-2015 standard safety test designed by China ensures the safe use of Li batteries to a certain extent.[152] The improvement strategies for the safety of Si anodes for LIBs involve two major approaches, i.e., microstructure engineering of Si anodes and the optimization of electrolytes and binders.[153] Microstructure engineering can alleviate the volume expansion of Si-based anodes, for instance, nanostructure and porous structure design. However, this strategy may also result in increased surface areas and, thereby, low initial CEs and irreversible

capacity loss.[154,155] Other effective measures have been applied to enhance Si anodes' safety, such as developing new binders[156] and electrolytes.[157,158]

Overall, achieving large-scale production, multifunctional composites, and good safety is vital to make further breakthroughs in commercialization of Si-based alloy anodes for next-generation high-energy secondary batteries.

Acknowledgements

The authors appreciate the funding support of the National Natural Science Foundation of China (Grant Nos. U2033206, 52222210, 51972067 and 51902062), and the Guangdong Natural Science Funds for Distinguished Young Scholar (Grant No. 2019B151502039).

Conflict of Interest

The authors declare that there are no conflict of interests.

Keywords: anode · commercialization · lithium-ion battery · microstructure engineering · silicon alloy

[1] J.-M. Tarascon, M. Armand, in *Materials for sustainable energy: a collection of peer-reviewed research and review articles from Nature Publishing Group*, World Scientific, **2011**, pp. 171–179.
[2] M. A. Pellow, H. Ambrose, D. Mulvaney, R. Betita, S. Shaw, *Sustain. Mater. Technol.* **2020**, *23*, e00120.
[3] G. Zubi, R. Dufo-López, M. Carvalho, G. Pasaoglu, *Renewable Sustainable Energy Rev.* **2018**, *89*, 292–308.
[4] V. Aravindan, Y. S. Lee, S. Madhavi, *Adv. Energy Mater.* **2015**, *5*, 1402225.
[5] S. W. Kim, D. H. Seo, X. Ma, G. Ceder, K. Kang, *Adv. Energy Mater.* **2012**, *2*, 710–721.
[6] Q. Li, X. Ye, H. Yu, C. Du, W. Sun, W. Liu, H. Pan, X. Rui, *Chin. Chem. Lett.* **2022**, *33*, 2663–2668.
[7] X. Zuo, J. Zhu, P. Müller-Buschbaum, Y.-J. Cheng, *Nano Energy* **2017**, *31*, 113–143.
[8] C. Dong, W. Dong, X. Lin, Y. Zhao, R. Li, F. Huang, *EnergyChem* **2020**, *2*, 100045.
[9] Y. Han, B. Liu, Z. Xiao, W. Zhang, X. Wang, G. Pan, Y. Xia, X. Xia, J. Tu, *InfoMat* **2021**, *3*, 155–174.
[10] Y. Liu, T. Matsumura, N. Imanishi, T. Ichikawa, A. Hirano, Y. Takeda, *Electrochem. Commun.* **2004**, *6*, 632–636.
[11] K. Hanai, Y. Liu, T. Matsumura, N. Imanishi, A. Hirano, Y. Takeda, *Solid State Ionics* **2008**, *179*, 1725–1730.
[12] Q. Shi, J. Zhou, S. Ullah, X. Yang, K. Tokarska, B. Trzebicka, H. Q. Ta, M. H. Ruemmeli, *Energy Storage Mater.* **2021**, *34*, 735–754.
[13] H. Ye, G. Zheng, X. Yang, D. Zhang, Y. Zhang, S. Yan, L. You, S. Hou, Z. Huang, *J. Electroanal. Chem.* **2021**, *898*, 115652.
[14] A. Franco Gonzalez, N.-H. Yang, R.-S. Liu, *J. Phys. Chem. C* **2017**, *121*, 27775–27787.
[15] B. Liang, Y. Liu, Y. Xu, *J. Power Sources* **2014**, *267*, 469–490.
[16] R. Teki, M. K. Datta, R. Krishnan, T. C. Parker, T. M. Lu, P. N. Kumta, N. Koratkar, *Small* **2009**, *5*, 2236–2242.
[17] H. Wu, Y. Cui, *Nano Today* **2012**, *7*, 414–429.
[18] J. R. Szczech, S. Jin, *Energy Environ. Sci.* **2011**, *4*, 56–72.
[19] C. K. Chan, R. Ruffo, S. S. Hong, Y. Cui, *J. Power Sources* **2009**, *189*, 1132–1140.
[20] Z.-y. Feng, W.-j. Peng, Z.-x. Wang, H.-j. Guo, X.-h. Li, G.-c. Yan, J.-x. Wang, *Int. J. Miner. Metall.* **2021**, *28*, 1549–1564.
[21] A. Casimir, H. Zhang, O. Ogoke, J. C. Amine, J. Lu, G. Wu, *Nano Energy* **2016**, *27*, 359–376.
[22] X. Li, M. Zhang, S. Yuan, C. Lu, *ChemElectroChem* **2020**, *7*, 4289–4302.
[23] F. Wang, G. Chen, N. Zhang, X. Liu, R. Ma, *Carbon Energy* **2019**, *1*, 219–245.
[24] Z. Zhang, X. Han, L. Li, P. Su, W. Huang, J. Wang, J. Xu, C. Li, S. Chen, Y. Yang, *J. Power Sources* **2020**, *450*, 227–593.
[25] Y. Yang, S. Wu, Y. Zhang, C. Liu, X. Wei, D. Luo, Z. Lin, *Chem. Eng. J.* **2021**, *406*, 126807.
[26] Y. An, H. Fei, G. Zeng, L. Ci, S. Xiong, J. Feng, Y. Qian, *ACS Nano* **2018**, *12*, 4993–5002.
[27] J. Li, Y. Cai, H. Wu, Z. Yu, X. Yan, Q. Zhang, T. Z. Gao, K. Liu, X. Jia, Z. Bao, *Adv. Energy Mater.* **2021**, *11*, 2003239.
[28] C. Zhang, F. Wang, J. Han, S. Bai, J. Tan, J. Liu, F. Li, *Small Structures* **2021**, *2*, 2100009.
[29] M. Sopicka-Lizer, *High-energy ball milling: mechanochemical processing of nanopowders*, Elsevier, **2010**.
[30] A. Stolle, T. Szuppa, S. E. Leonhardt, B. Ondruschka, *Chem. Soc. Rev.* **2011**, *40*, 2317–2329.
[31] P. J. Kelly, R. D. Arnell, *Vacuum* **2000**, *56*, 159–172.
[32] U. Seyfert, U. Heisig, G. Teschner, J. Strümpfel, *SVC Bull. Fall.* **2015**, *2015*, 22–26.
[33] D. B. Chrisey, G. K. Hubler, in *Pulsed Laser Deposition of Thin Films*, John Wiley & Sons, Inc., New York, **1994**.
[34] R. Eason, *Pulsed laser deposition of thin films: applications-led growth of functional materials*, John Wiley & Sons, **2007**.
[35] J. Singh, D. E. Wolfe, *J. Mater. Sci.* **2005**, *40*, 1–26.
[36] A. A. Dinata, A. M. Rosyadi, S. Hamid, R. Zainul, **2018**.
[37] S. R. Nagel, J. B. MacChesney, K. L. Walker, *IEEE Trans. Microwave Theory Tech.* **1982**, *30*, 305–322.
[38] C. Zhu, Y. Fu, Y. Yu, *Adv. Mater.* **2019**, *31*, 1803408.
[39] M. Tyona, *Adv. Mater. Res.* **2013**, *2*, 195.
[40] H. A. M. Mustafa, D. A. Jameel, *J. Appl. Sci. Technol. Trends.* **2021**, *2*, 91–95.
[41] A. D. McNaught, A. Wilkinson, **1997**.
[42] M. K. Beyer, H. Clausen-Schaumann, *Chem. Rev.* **2005**, *105*, 2921–2948.
[43] V. V. Boldyrev, *Russ. Chem. Rev.* **2006**, *75*, 177.
[44] G. Kaupp, *CrystEngComm* **2009**, *11*, 388–403.
[45] L. Wang, D. Ma, C. Guo, X. Jiang, M. Li, T. Xu, J. Zhu, B. Fan, W. Liu, G. Shao, *Appl. Surf. Sci.* **2021**, *543*, 148782.
[46] C. Suryanarayana, *Prog. Mater. Sci.* **2001**, *46*, 1–184.
[47] D. Duveau, B. Fraisse, F. d r Cunin, L. Monconduit, *Chem. Mater.* **2015**, *27*, 3226–3233.
[48] G. Le Caër, P. Delcroix, S. Bégin-Colin, T. Ziller, *Hyperfine Interact.* **2002**, *141*, 63–72.
[49] B. Kieback, H. Kubsch, A. Bunke, *J. Phys. IV Proc.* **1993**, *3*, 1425–1428.
[50] G. Wang, L. Sun, D. Bradhurst, S. Zhong, S. Dou, H. Liu, *J. Alloys Compd.* **2000**, *306*, 249–252.
[51] M.-S. Park, Y.-J. Lee, S. Rajendran, M.-S. Song, H.-S. Kim, J.-Y. Lee, *Electrochim. Acta.* **2005**, *50*, 5561–5567.
[52] K.-M. Lee, Y.-S. Lee, Y.-W. Kim, Y.-K. Sun, S.-M. Lee, *J. Alloys Compd.* **2009**, *472*, 461–465.
[53] H.-Y. Lee, S.-M. Lee, *J. Power Sources* **2002**, *112*, 649–654.
[54] C.-M. Hwang, J.-W. Park, *Electrochim. Acta* **2011**, *56*, 6737–6747.
[55] T. Zhang, L. Fu, *Chem* **2018**, *4*, 671–689.
[56] H. Wolf, Z. Pajkic, T. Gerdes, M. Willert-Porada, *J. Power Sources* **2009**, *190*, 157–161.
[57] D. M. Mattox, *Handbook of physical vapor deposition (PVD) processing*, William Andrew, **2010**.
[58] J. Carlsson, P. Martin, *Science, Technology and Applications* **2010**, 444–445.
[59] K. Holmberg, A. Matthews, *Coatings tribology: properties, mechanisms, techniques and applications in surface engineering*, Elsevier, **2009**.
[60] M. Singh M, H. Kumar, P. Sivaiah, *Int. J. Thin Film Sci. Technol.* **2021**, *10*, 3.
[61] A. Baptista, F. Silva, J. Porteiro, J. Míguez, G. Pinto, L. Fernandes, *Procedia Manuf.* **2018**, *17*, 746–757.
[62] S. Hogmark, S. Jacobson, M. Larsson, *Wear* **2000**, *246*, 20–33.
[63] X. Jiang, F.-C. Yang, W.-C. Chen, J.-W. Lee, C.-L. Chang, *Surf. Coat. Technol.* **2017**, *320*, 138–145.
[64] J. Zhang, Z.-L. Hou, X. Zhang, C. Li, *Int. J. Hydrogen Energy* **2022**, *47*, 4766–4771.
[65] E. Harris, *Phys. Rev. Lett.* **1959**, *2*, 34.
[66] J.-Y. Woo, A.-Y. Kim, M. K. Kim, S.-H. Lee, Y.-K. Sun, G. Liu, J. K. Lee, *J. Alloys Compd.* **2017**, *701*, 425–432.
[67] M. W. Forney, R. A. DiLeo, A. Raisanen, M. J. Ganter, J. W. Staub, R. E. Rogers, R. D. Ridgley, B. J. Landi, *J. Power Sources* **2013**, *228*, 270–280.

[68] J. Jang, I. Kang, K.-W. Yi, Y. W. Cho, *Appl. Surf. Sci.* **2018**, *454*, 277–283.
[69] H. O. Pierson, *Handbook of chemical vapor deposition: principles, technology and applications*, William Andrew, **1999**.
[70] C.-M. Park, J.-H. Kim, H. Kim, H.-J. Sohn, *Chem. Soc. Rev.* **2010**, *39*, 3115–3141.
[71] X. Cao, Q. Li, Y. Shi, D. Wu, X. Xue, *Metals* **2020**, *10*, 1067.
[72] J. Zhao, X. Qu, J. Qu, B. Zhang, Z. Ning, H. Xie, X. Zhou, Q. Song, P. Xing, H. Yin, *J. Hazard. Mater.* **2019**, *379*, 120817.
[73] Y. Gao, M. Peng, Y. Sun, Y. Yang, X. Wang, *Optoelectron. Adv. Mater. Rapid Commun.* **2015**, *9*, 245–247.
[74] L. Dai, Y. Yu, H. Zhou, X. Yan, J. Zhu, Y. Li, L. Wang, *Ceram. Int.* **2015**, *41*, 13663–13670.
[75] J. Cheng, J. Qiao, Z. Yang, B. Zhu, J. Duan, D. Wang, R. Huang, Y. Zhang, Z. Zhou, P. Dong, *J. Alloys Compd.* **2022**, *890*, 161732.
[76] P. R. Coxon, M. Coto, E. Juzeliunas, D. J. Fray, *Prog. Nat. Sci.* **2015**, *25*, 583–590.
[77] X. Li, C. Wang, *J. Mater. Chem. A* **2013**, *1*, 165–182.
[78] L. L. Hench, J. K. West, *Chem. Rev.* **1990**, *90*, 33–72.
[79] N. Bhardwaj, S. C. Kundu, *Biotechnol. Adv.* **2010**, *28*, 325–347.
[80] A. Huang, Y. Ma, J. Peng, L. Li, S.-I. Chou, S. Ramakrishna, S. Peng, *eScience* **2021**, *1*, 141–162.
[81] B. Polat, O. Keles, Z. Chen, K. Amine, *J. Mater. Sci.* **2016**, *51*, 6207–6219.
[82] K. Stokes, H. Geaney, G. Flynn, M. Sheehan, T. Kennedy, K. M. Ryan, *ACS Nano* **2017**, *11*, 10088–10096.
[83] J. Sun, J. Li, B. Ban, J. Shi, Q. Wang, J. Chen, *Electrochim. Acta* **2020**, *345*, 136242.
[84] J. Wang, N. Du, Z. Song, H. Wu, H. Zhang, D. Yang, *J. Power Sources* **2013**, *229*, 185–189.
[85] Y. Yang, S. Liu, X. Bian, J. Feng, Y. An, C. Yuan, *ACS Nano* **2018**, *12*, 2900–2908.
[86] Y.-L. Kim, H.-Y. Lee, S.-W. Jang, S.-H. Lim, S.-J. Lee, H.-K. Baik, Y.-S. Yoon, S.-M. Lee, *Electrochim. Acta.* **2003**, *48*, 2593–2597.
[87] P. R. Abel, A. M. Chockla, Y.-M. Lin, V. C. Holmberg, J. T. Harris, B. A. Korgel, A. Heller, C. B. Mullins, *ACS Nano* **2013**, *7*, 2249–2257.
[88] M. Fleischauer, M. Obrovac, J. Dahn, *J. Electrochem. Soc.* **2008**, *155*, A851.
[89] G. Wang, L. Sun, D. Bradhurst, S. Zhong, S. Dou, H. Liu, *J. Power Sources* **2000**, *88*, 278–281.
[90] Z. Du, S. Ellis, R. Dunlap, M. Obrovac, *J. Electrochem. Soc.* **2015**, *163*, A13.
[91] H. Wang, S. Fan, Y. Cao, H. Yang, X. Ai, F. Zhong, *ACS Appl. Mater. Interfaces* **2020**, *12*, 30503–30509.
[92] W. Li, X. Li, J. Liao, B. Zhao, L. Zhang, L. Huang, G. Liu, Z. Guo, M. Liu, *Energy Environ. Sci.* **2019**, *12*, 2286–2297.
[93] H. Kim, Y. Son, C. Park, M.-J. Lee, M. Hong, J. Kim, M. Lee, J. Cho, H. C. Choi, *Nano Lett.* **2015**, *15*, 4135–4142.
[94] H.-I. Park, M. Sohn, J.-H. Choi, C. Park, J.-H. Kim, H. Kim, *Electrochim. Acta.* **2016**, *210*, 301–307.
[95] P. Zhang, L. Huang, Y. Li, X. Ren, L. Deng, Q. Yuan, *Electrochim. Acta* **2016**, *192*, 385–391.
[96] Z. Chen, X. Wang, T. Jian, J. Hou, J. Zhou, C. Xu, *Solid State Ionics* **2020**, *354*, 115406.
[97] N. Bensalah, M. Matalkeh, N. K. Mustafa, H. Merabet, *Phys. Status Solidi* **2020**, *217*, 1900414.
[98] H. Zhang, H. Xu, X. Lou, H. Jin, P. Zong, S. Li, Y. Bai, F. Ma, *Ionics* **2019**, *25*, 4667–4673.
[99] G. Schmuelling, M. Winter, T. Placke, *ACS Appl. Mater. Interfaces* **2015**, *7*, 20124–20133.
[100] H. Wu, P. Gao, J. Mu, Z. Miao, P. Zhou, T. Zhou, J. Zhou, *Chin. Chem. Lett.* **2022**, *33*, 3236–3240.
[101] D. Wang, M. Gao, H. Pan, J. Wang, Y. Liu, *J. Power Sources* **2014**, *256*, 190–199.
[102] S. Goriparti, E. Miele, F. De Angelis, E. Di Fabrizio, R. P. Zaccaria, C. Capiglia, *J. Power Sources* **2014**, *257*, 421–443.
[103] X. Su, Q. Wu, J. Li, X. Xiao, A. Lott, W. Lu, B. W. Sheldon, J. Wu, *Adv. Energy Mater.* **2014**, *4*, 1300882.
[104] A. Y. Galashev, *Solid State Ionics* **2020**, *357*, 115463.
[105] R. Beyers, R. Sinclair, *J. Alloys Compd.* **1985**, *57*, 5240–5245.
[106] Y.-S. Lee, J.-H. Lee, Y.-W. Kim, Y.-K. Sun, S.-M. Lee, *Electrochim. Acta.* **2006**, *52*, 1523–1526.
[107] Y. Wang, S. Cao, M. Kalinina, L. Zheng, L. Li, M. Zhu, M. Obrovac, *J. Electrochem. Soc.* **2017**, *164*, A3006.
[108] P. Mondal, A. Anweshan, M. K. Purkait, *Chemosphere* **2020**, *259*, 127509.
[109] M. Ruttert, V. Siozios, M. Winter, T. Placke, *ACS Appl. Energ. Mater.* **2019**, *3*, 743–758.
[110] X. Li, Y. Zheng, Z. Li, Y. Liu, H. Huang, Q. Wang, C. Dong, *Mater. Chem. Phys.* **2020**, *243*, 122666.
[111] K. Lee, J. Jeong, Y. Chu, J. Kim, K. Oh, J. Moon, *Materials* **2022**, *15*, 1873.
[112] H. Liu, Y. Long, Y. Chen, Z. Wang, C. Zhang, R. Hu, X. Zhang, P. Yu, *ACS Appl. Mater. Interfaces* **2021**, *13*, 57317–57325.
[113] B.-S. Lee, H.-S. Yang, K. H. Lee, S. Han, W.-R. Yu, *Energy Storage Mater.* **2019**, *17*, 62–69.
[114] D. Li, H. Wang, T. Zhou, W. Zhang, H. K. Liu, Z. Guo, *Adv. Energy Mater.* **2017**, *7*, 1700488.
[115] D. Puthusseri, M. Wahid, S. Ogale, *ACS Omega* **2018**, *3*, 4591–4601.
[116] H. Wang, H. Huang, C. Niu, A. L. Rogach, *Small* **2015**, *11*, 1364–1383.
[117] Z. Xu, T. Yang, X. Chu, H. Su, Z. Wang, N. Chen, B. Gu, H. Zhang, W. Deng, H. Zhang, W. Yang, *ACS Appl. Mater. Interfaces* **2020**, *12*, 10341–10349.
[118] M. R. Zamfir, H. T. Nguyen, E. Moyen, Y. H. Lee, D. Pribat, *J. Mater. Chem. A* **2013**, *1*, 9566–9586.
[119] D. Wang, Y.-L. Chang, Q. Wang, J. Cao, D. B. Farmer, R. G. Gordon, H. Dai, *J. Am. Chem. Soc.* **2004**, *126*, 11602–11611.
[120] D. Li, H. Wang, H. K. Liu, Z. Guo, *Adv. Energy Mater.* **2016**, *6*, 1501666.
[121] V. A. Sethuraman, K. Kowolik, V. Srinivasan, *J. Power Sources* **2011**, *196*, 393–398.
[122] K. S. Novoselov, A. K. Geim, S. V. Morozov, D. Jiang, M. I. Katsnelson, I. Grigorieva, S. Dubonos, a. Firsov, *Nature* **2005**, *438*, 197–200.
[123] C. Meng, P. Das, X. Shi, Q. Fu, K. Müllen, Z.-S. Wu, *Small Sci.* **2021**, *1*, 2000076.
[124] L. Wang, W. Guo, P. Lu, T. Zhang, F. Hou, J. Liang, *Front. Chem.* **2019**, 832.
[125] X. Zhang, S. Li, J. Li, M. Ye, Z. Song, S. Jin, B. Shi, Y. Pan, J. Yan, Y. Wang, *Comput. Condens. Matter* **2019**, *21*, e00404.
[126] X. Han, L. Sun, F. Wang, D. Sun, *J. Mater. Chem. A* **2018**, *6*, 18891–18897.
[127] J. Jia, B. Li, S. Duan, Z. Cui, H. Gao, *Nanoscale* **2019**, *11*, 20307–20314.
[128] H. g Wang, Q. Wu, Y. Wang, X. Wang, L. Wu, S. Song, H. Zhang, *Adv. Energy Mater.* **2019**, *9*, 1802993.
[129] X. Sun, S. Wu, K. N. Dinh, Z. Wang, *J. Solid State Chem.* **2019**, *274*, 265–269.
[130] P. Zhu, Y. Zu, Y. Kuai, S. Gao, G. Wu, W. Chen, L. Wu, C. Chen, G. Liu, *Phys. Chem. Chem. Phys.* **2021**, *23*, 26428–26437.
[131] Q. He, B. Yu, Z. Li, Y. Zhao, *Energy Environ. Mater.* **2019**, *2*, 264–279.
[132] M. Ge, X. Fang, J. Rong, C. Zhou, *Nanotechnology* **2013**, *24*, 422001.
[133] K. Peng, J. Jie, W. Zhang, S.-T. Lee, *Appl. Phys. Lett.* **2008**, *93*, 033105.
[134] C. K. Chan, H. Peng, G. Liu, K. Mcllwrath, X. F. Zhang, R. A. Huggins, Y. Cui, *Nat. Nanotechnol.* **2008**, *3*, 31–35.
[135] Y.-N. Zhou, M.-Z. Xue, Z.-W. Fu, *J. Power Sources* **2013**, *234*, 310–332.
[136] A. Reyes Jiménez, R. Klöpsch, R. Wagner, U. C. Rodehorst, M. Kolek, R. Nölle, M. Winter, T. Placke, *ACS Nano* **2017**, *11*, 4731–4744.
[137] M. Schmerling, J. Schwenzel, M. Busse, *Thin Solid Films* **2018**, *655*, 77–82.
[138] G.-B. Cho, J.-K. Kim, S.-H. Lee, G.-T. Kim, J.-P. Noh, K.-K. Cho, K.-W. Kim, T.-H. Nam, H.-J. Ahn, *Electrochim. Acta* **2017**, *224*, 649–659.
[139] M. Salah, P. Murphy, C. Hall, C. Francis, R. Kerr, M. Fabretto, *J. Power Sources* **2019**, *414*, 48–67.
[140] C. Yu, X. Li, T. Ma, J. Rong, R. Zhang, J. Shaffer, Y. An, Q. Liu, B. Wei, H. Jiang, *Adv. Energy Mater.* **2012**, *2*, 68–73.
[141] H. Zhang, H. Xu, *Solid State Ionics* **2014**, *263*, 23–26.
[142] X. Huang, F. Zhang, X. Gan, Q. Huang, J. Yang, P. Lai, W. Tang, *RSC Adv.* **2018**, *8*, 5189–5196.
[143] G. Schmuelling, M. Winter, T. Placke, *ACS Appl. Mater. Interfaces* **2015**, *7*, 20124–20133.
[144] H. Jiang, X. Zhou, G. Liu, Y. Zhou, H. Ye, Y. Liu, K. Han, *Electrochim. Acta* **2016**, *188*, 777–784.
[145] C. Liu, J. Sun, P. Zheng, L. Jiang, H. Liu, J. Chai, Q. Liu, Z. Liu, Y. Zheng, X. Rui, *J. Mater. Chem. A* **2022**, *10*, 16761–16778.
[146] S.-M. Zheng, Y.-R. Tian, Y.-X. Liu, S. Wang, C.-Q. Hu, B. Wang, K.-M. Wang, *Rare Met.* **2021**, *40*, 272–289.
[147] K. Song, C. Liu, L. Mi, S. Chou, W. Chen, C. Shen, *Small* **2021**, *17*, 1903194.
[148] Q. Ma, Y. Dai, H. Wang, G. Ma, H. Guo, X. Zeng, N. Tu, X. Wu, M. Xiao, *Chin. Chem. Lett.* **2021**, *32*, 5–8.
[149] A. Louli, J. Li, S. Trussler, C. R. Fell, J. Dahn, *J. Electrochem. Soc.* **2017**, *164*, A2689.

[150] Y. Jia, J. Li, C. Yuan, X. Gao, W. Yao, M. Lee, J. Xu, *Adv. Energy Mater.* **2021**, *11*, 2003868.
[151] Y. Wu, Y. Wang, W. K. Yung, M. Pecht, *Electronics* **2019**, *8*, 751.
[152] B. Kotak, Y. Kotak, K. Brade, T. Kubjatko, H.-G. Schweiger, *Batteries* **2021**, *7*, 63.
[153] F. Wang, P. Zhang, G. Wang, A. S. Nia, M. Yu, X. Feng, *Small Sci.* **2022**, *2*, 2100080.
[154] L. Sun, Y. Liu, R. Shao, J. Wu, R. Jiang, Z. Jin, *Energy Storage Mater.* **2022**, *46*, 482–502.
[155] Q. Liu, T. Meng, L. Yu, S. Guo, Y. Hu, Z. Liu, X. Hu, *Small Methods* **2022**, 2200380.
[156] S. Wu, Y. Yang, C. Liu, T. Liu, Y. Zhang, B. Zhang, D. Luo, F. Pan, Z. Lin, *ACS Energy Lett.* **2020**, *6*, 290–297.
[157] J. Wang, Y. Cui, *Nat. Energy* **2020**, *5*, 361–362.
[158] S. Zhang, S. Li, Y. Lu, *eScience* **2021**, *1*, 163–177.

Manuscript received: November 7, 2022
Accepted manuscript online: November 9, 2022
Version of record online: November 30, 2022